Interatomic interaction effects on second-order momentum correlations and Hong-Ou-Mandel interference of double-well-trapped ultracold fermionic atoms

Benedikt B. Brandt,* Constantine Yannouleas,† and Uzi Landman‡
School of Physics, Georgia Institute of Technology, Atlanta, Georgia 30332-0430, USA

(Received 2 January 2018; published 4 May 2018)

Identification and understanding of the evolution of interference patterns in two-particle momentum correlations as a function of the strength of interatomic interactions are important in explorations of the nature of quantum states of trapped particles. Together with the analysis of two-particle spatial correlations, they offer the prospect of uncovering fundamental symmetries and structure of correlated many-body states, as well as opening vistas into potential control and utilization of correlated quantum states as quantum-information resources. With the use of the second-order density matrix constructed via exact diagonalization of the microscopic Hamiltonian, and an analytic Hubbard-type model, we explore here the systematic evolution of characteristic interference patterns in the two-body momentum and spatial correlation maps of two entangled ultracold fermionic atoms in a double well, for the entire attractive- and repulsive-interaction range. We uncover quantum-statistics-governed bunching and antibunching, as well as interaction-dependent interference patterns, in the ground and excited states, and interpret our results in light of the Hong-Ou-Mandel interference physics, widely exploited in photon indistinguishability testing and quantum-information science.

DOI: 10.1103/PhysRevA.97.053601

I. INTRODUCTION

The rapid experimental progress in the field of ultracold atoms is enabling measurements with unprecedented precision of fundamental many-body quantities such as higher-order correlations [1–7], especially higher-order *momentum* correlations for interacting [4,5,7] ultracold atoms in linear traps. The study of these correlations, with the full ability of tuning the interparticle interactions (utilizing the Feshbach resonance technique) and under pristine environmental conditions, promises to deepen our understanding and potential technological control of quantum-information processes [8] and physical phenomena, such as entanglement [9] and generation of exotic many-body regimes (e.g., Tonks-Girardeau states [10]). However, in spite of the recent burgeoning experimental activities aimed at measuring higher-order momentum correlations [4–7], corresponding theoretical investigations are still lacking in many respects, apart from a couple of studies [4,11].

In this paper, we study the systematic evolution of the properties and interference patterns of second-order (two-particle) momentum correlations of two interacting (both distinguishable and indistinguishable) ultracold fermions in a double-well optical trap. To provide a complete picture, we go beyond the case of the ground singlet and first-excited triplet states and investigate in addition the cases of the second- and third-excited states, both singlets. (This quartet of states can be mapped to a two-site Hubbard model; see below.)

Elucidating the second-order momentum correlations associated with double-well trapping of two ultracold atoms (without [6] or with [7] interactions) is currently attracting pioneering experimental interest, both planned [6] and preparatorily achieved [7]. These experimental efforts are motivated by the unprecedented tunability of (i) the confining external optical potential and the dynamical imprinting of a relative phase difference between the two wells [6], and (ii) the two-body contact interaction via a combination of Feshbach and confinement-induced resonances [12,13].

The double-well two-particle unit [13,14] is expected to be a central component for building more complex quantum-computer and quantum-information architectures, and detailed knowledge of the associated second-order momentum correlations is emerging as an indispensable tool towards implementation of these endeavors [6,7]. In this context, recent work [3,6] investigates the double-well atomic dimers, treating them as purely photonic analogs (i.e., omitting or minimizing the role of interparticle interaction). The interparticle interaction, however, is an essential factor in particle assemblies and the desirability of a full understanding of its effects can hardly be overestimated. The seminal optical Hong-Ou-Mandel (HOM) second-order-interference experiment [15,16], widely exploited in photon indistinguishability testing and quantum-information science, spawned extensions of such interference phenomena to electrons [17,18] and bosonic atoms [3,19]. Here we further interpret our correlation results for ultracold fermions in light of the HOM physics.

The much-sought-after deeper understanding of the double-well fermionic dimer is achieved below through employment of an exact configuration-interaction (CI) method for solving the two-body problem, in conjunction with a modified Hubbard-type analytic modeling that allows a synoptic interpretation of the properties and interference patterns of the microscopic, numerically CI-derived, two-particle momentum correlations.

The paper is organized as follows. In Sec. II, essential definitions and theoretical details are given. Section III displays a detailed analysis pertaining mainly to interatomic interaction

*benbra@gatech.edu
†constantine.yannouleas@physics.gatech.edu
‡uzi.landman@physics.gatech.edu

 ©2018 American Physical Society

effects on the CI-calculated and Hubbard-type-modeled patterns for the second-order (two-body) spatial and momentum correlation distribution maps obtained for the ground state of two fermionic atoms trapped in a double well. Microscopic (CI) and Hubbard-like analysis of second-order correlation maps for the excited states is given in Sec. IV. Section V links our microscopically calculated and analytically (Hubbard-type) derived momentum correlation results with the Hong-Ou-Mandel interference physics, uncovering quantum-statistics-governed (spatial symmetry of the two-particle wave function) and interaction-dependent bunching and antibunching behavior, as well as other interference patterns, in the ground and excited states. We summarize our results in Sec. VI. The appendices give details of the derivation of analytic Hubbard-type two-particle interference formulas (Appendix A), the methodology of extraction of Hubbard-model parameters from the CI calculations (Appendix B), and further illustrations of Hubbard-model-derived two-particle momentum correlation maps (Appendix C). Appendix D displays the derivation and analytical expressions for the two-body density matrices for the ground and excited states corresponding to the Hubbard-type model described in Appendix A, and relates these to the second-order momentum correlation maps discussed in the paper.

II. THEORY ESSENTIALS

To implement the microscopic CI method, we start by considering the two-dimensional (2D) Hamiltonian of two interacting ultracold fermions,

$$H_{\rm MB} = H(1) + H(2) + V(\mathbf{r}_1,\mathbf{r}_2), \tag{1}$$

where $H(i)$ represents the single-particle part of the many-body Hamiltonian and $V(\mathbf{r}_1,\mathbf{r}_2)$ represents the interaction term, with $\mathbf{r}_i \equiv (x_i,y_i)$, $i = 1,2$, being the space coordinates of the first and second particle. The single-particle part $H(i)$ of the Hamiltonian contains the kinetic-energy term and a single-particle external confining potential; in this paper, we consider a double-well confinement.

The double-well external confining potential has been extensively described in Refs. [14,20]. The relevant potential parameters are the interwell separation $2d = d_2 - d_1$ ($d_1 < d_2$) along the x direction, and the value of the dimensionless parameter ϵ_b (determining the interwell barrier height V_b) is taken to be 0.5 throughout the paper. Each of the parabolic confining wells is characterized by two harmonic frequencies, ω_x (along the x axis of the well) and ω_y (along the y direction), resulting in a (quasi-one-dimensional) needlelike shape confinement when $\omega_x << \omega_y$. In our calculations here, we consider two different sets of values, i.e., $\omega_x = 2\pi \times 8$, $\omega_y = 2\pi \times 800$ kHz and $\omega_x = 2\pi \times 15$, $\omega_y = 2\pi \times 1500$ kHz, both having the same aspect ratio ω_x/ω_y; hereafter we drop, for convenience, the subscript x and use $\omega = \omega_x$.

The short-range interatomic interaction term is given by

$$V(\mathbf{r}_1,\mathbf{r}_2) = \frac{g}{\sigma^2\pi} e^{-(\mathbf{r}_1-\mathbf{r}_2)^2/\sigma^2}. \tag{2}$$

In this paper, we use $\sigma = 0.01$ μm, yielding a ratio $\sigma/l_0 \sim 0.03$ for the case of $\omega = 2\pi \times 8$ kHz and $\sigma/l_0 \sim 0.022$ for the case of $\omega = 2\pi \times 15$ kHz; l_0 is the oscillator length $l_0^2 = \hbar/(M_{^6\rm Li}\omega)$, with $M_{^6\rm Li} = 10964.90 m_e$ being the mass of ^{6}Li; a pair of states out of the three lowest ^{6}Li hyperfine states corresponds to two different spin states [12]. The factors σ/l_0 are motivated by the need to model short-range, contact-type interactions. Any Gaussian width σ that is sufficiently smaller than the harmonic-oscillator length l_0 along the x direction is suitable and yields essentially identical final results. Here we consider both mutually repelling ($g > 0$) and attractive ($g < 0$) particles and the tunable values of the interaction strength g will be given in units of $\hbar\omega l_0^2$.

Because for $N = 2$ fermions the spin variables separate from the space variables [21], the CI wave function has the product form $\Phi_{\rm CI}^{S,S_z}(\mathbf{r}_1,\mathbf{r}_2)\chi(S,S_z)$, where S and S_z denote the total spin and its projection. As a result, for $N = 2$, the spin-resolved and spin-unresolved two-body correlations are the same [11], apart from an overall factor. Then the two-body space correlation is defined by [11]

$$\mathcal{P}_{\rm CI}^{S,S_z}(\mathbf{r}_1,\mathbf{r}_1',\mathbf{r}_2,\mathbf{r}_2') = \Phi_{\rm CI}^{S,S_z\dagger}(\mathbf{r}_1,\mathbf{r}_1')\Phi_{\rm CI}^{S,S_z}(\mathbf{r}_2,\mathbf{r}_2'), \tag{3}$$

while the two-body momentum correlation is given by the Fourier transform,

$$\mathcal{G}_{\rm CI}^{S,S_z}(\mathbf{k}_1,\mathbf{k}_2) = \frac{1}{4\pi^2}\int_{-\infty}^{\infty} e^{-i\mathbf{k}_1\cdot(\mathbf{r}_1-\mathbf{r}_1')}\int_{-\infty}^{\infty} e^{-i\mathbf{k}_2\cdot(\mathbf{r}_2-\mathbf{r}_2')} \times \mathcal{P}_{\rm CI}^{S,S_z}(\mathbf{r}_1,\mathbf{r}_1',\mathbf{r}_2,\mathbf{r}_2')d\mathbf{r}_1 d\mathbf{r}_1' d\mathbf{r}_2 d\mathbf{r}_2'. \tag{4}$$

III. ANALYSIS OF THE GROUND STATE

In Fig. 1, we plot the CI two-body correlations for two repelling fermions in their singlet ($S = 0, S_z = 0$) ground state as a function of the interaction strength g (in units of $\hbar\omega l_0^2$); the interwell separation is $2d = 2$ μm. The values of g are also expressed as the ratio U/t between the on-site repulsion (U) and the intersite hopping parameter (t) associated with the two-site Hubbard model (whose parameters have been extracted from the microscopic CI calculation; see Appendix B). Two different confining harmonic potentials have been considered with energy spacings $\omega = 2\pi \times 8$ kHz (top row) and $\omega = 2\pi \times 15$ kHz (bottom row). In all cases in this work, we show two-particle spatial correlation maps for $y_1 = y_2 = 0$ and two-particle momentum correlation maps for $k_1^y = k_2^y = 0$; we verified that similar results are obtained for other $y_1 = y_2 =$ const and $k_1^y = k_2^y =$ const values. Note that we drop, for convenience, the superscript x and use $k_i = k_i^x$, where $i = 1,2$ denotes the index numbering the two particles.

The spatial correlations for the above-noted two confining-potential energy spacings [Figs. 1(a), 1(c) 1(e), 1(g) and Figs. 1(i), 1(k) 1(m), 1(o), respectively] exhibit similar behavior as g (or U/t) increases, transforming from a four-hump pattern in a square formation to a two-hump one along the $x_1 + x_2 = 0$ diagonal (referred to here as "antidiagonal"). Naturally, in the noninteracting limit [$g \sim 0$, $U/t \sim 0$; Figs. 1(a) and 1(i)], the two humps located along the $x_1 - x_2 = 0$ diagonal (referred to here as "main diagonal") are due to the double occupancy (involving both the $\uparrow$ and $\downarrow$ spins) of the lowest symmetric single-particle orbital of the double well, which in the Hubbard modeling translates into double occupancy of each site. As g increases, the double-occupancy humps along the main diagonal progressively shrink, and they eventually

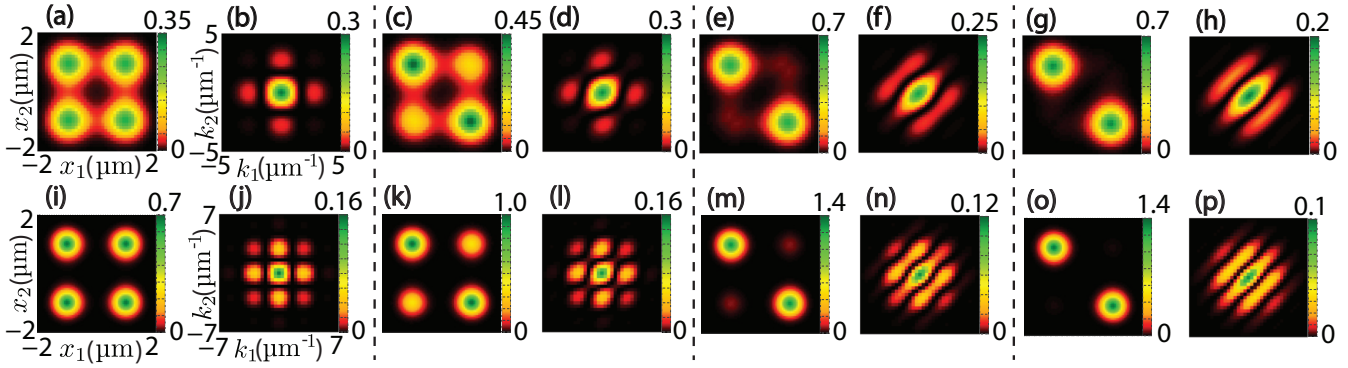

FIG. 1. Ground-state CI-calculated spatial and momentum correlation maps for two fermions in a double well, as a function of the two-body interaction strength g. The interwell distance is $2d = 2\,\mu$m; in the real-space correlation maps we take the origin midway between the two wells, with the wells located one at $d_1 = -d$ and the other at $d_2 = d > 0$ (in particular, here $d = 1\,\mu$m). The results in the upper and lower rows correspond to two different choices of the confining harmonic frequencies along the interwell direction (x) and in the transverse one (y). The top row shows results for $\omega_x = 2\pi \times 8$ kHz and the bottom row shows results for $\omega_x = 2\pi \times 15$ kHz; for both cases, $\omega_x/\omega_y = 1/100$. The results in (a),(b) and (i),(j) are for an interaction strength $g = 5.5 \times 10^{-6}$ [in units of $\hbar\omega l_0^2$; see text after Eq. (2)], corresponding to a Hubbard parameter $U/t = 0$ (that is, noninteracting particles); those in (c),(d) and (k),(l) are for $g = 3.1 \times 10^{-2}$ and $g = 1.2 \times 10^{-3}$, respectively, corresponding to $U/t = 2$; the ones in (e),(f) and (m),(n) are for $g = 1.3 \times 10^{-1}$ and $g = 4.8 \times 10^{-3}$, respectively, corresponding to $U/t = 8$; and in (g),(h) and (o),(p), they are for $g = 3.1 \times 10^{-1}$ and $g = 1.2 \times 10^{-2}$, respectively, corresponding to $U/t = 20$. Because of the quasilinear nature of the system, here and for all 2D CI-derived correlations, the maps are drawn for $y_1 = y_2 = 0$ for the spatial correlations and for $k_1^y = k_2^y = 0$ for the momentum correlations. Note that we drop, for convenience, the superscript x and use $k_i = k_i^x$, where $i = 1,2$ denotes the index numbering the two particles. This yields the plotted correlation maps for the position (x_1,x_2) and momentum (k_1,k_2) variables along the x direction connecting the two wells. The color scale, corresponding to the values in the correlation maps, is given by the vertical bar to the right of each of the frames.

vanish in the strong-repulsion regime [see case for $U/t = 20$ in Figs. 1(g) and 1(o)].

The evolution of the two-body momentum correlations [Figs. 1(b), 1(d) 1(f), 1(h) and Figs. 1(j), 1(l) 1(n), 1(p)] is more complex. At the noninteracting limit [Figs. 1(b) and 1(j)], a plaid pattern of circular humps is evident. As a function of increasing g, the plaid pattern distorts and transforms into interference fringes exhibiting elongated maxima along and parallel to the main diagonal ($k_1 - k_2 = 0$); the associated valleys (minima) of this pattern appear along the antidiagonal ($k_1 + k_2 = 0$). This interference pattern is well developed for $U/t = 20$ for which the residues of the $U = 0$ circular humps only minimally distort the parallel fringes. We checked that the $U = 0$ circular humps do not survive for larger values of g (or U/t).

Furthermore, there is a prominent qualitative difference between the top-row ($\omega = 2\pi \times 8$ kHz confinement) and bottom-row ($\omega = 2\pi \times 15$ kHz confinement) momentum maps. Indeed, for $\omega = 2\pi \times 15$ kHz (bottom row), there are more individual features (humps or fringes) compared to the case of $\omega = 2\pi \times 8$ kHz (top row). In particular, we note for the independent particle case that there are nine visible humps in Fig. 1(j) compared to four humps in Fig. 1(b), with the additional maxima in Fig. 1(j) revealing for $U = 0$ enhanced correlations between particles with equal momenta, regardless of their signs. Similarly, for $U/t = 20$, we find five visible fringes in Fig. 1(p) compared to three in Fig. 1(h), with the added fringes in Fig. 1(p) revealing correlations between particles having the same, but of opposite sign, momenta.

To gain insights about the systematics in the evolution of the momentum maps, we model the fermion single-particle space orbitals as displaced Gaussian functions centered at each well. Taking account of the spin, the ensuing Gaussian-type spin orbitals are used to form Slater determinants according to the spin eigenfunctions of the corresponding two-site Hubbard model (with parameters U and t extracted from the CI calculations; see Appendix B). This procedure endows the Hubbard-model eigenvector solutions with the (otherwise absent) spatial degrees of freedom; see Appendix A. Considering the strictly one-dimensional case along the x axis and applying the definition in Eq. (4) to these modified Hubbard-model solutions, one obtains, for the two-body momentum correlation of the singlet ground state,

$$\mathcal{G}^{S=0,S_z=0}_{\mathrm{Hub,gs}}(k_1,k_2) \propto \frac{2s^2 e^{-2s^2(k_1^2+k_2^2)}}{\pi[\mathcal{U}\mathcal{Q}(\mathcal{U})+16]} \times \{[\mathcal{U}\mathcal{Q}(\mathcal{U})+8]\cos[2d(k_1-k_2)] + 8\cos[2d(k_1+k_2)] + 4\mathcal{Q}(\mathcal{U})\cos(2dk_1) + 4\mathcal{Q}(\mathcal{U})\cos(2dk_2) + \mathcal{U}\mathcal{Q}(\mathcal{U}) + 16\}, \tag{5}$$

where $\mathcal{U} = U/t$, $\mathcal{Q}(\mathcal{U}) = \sqrt{\mathcal{U}^2+16} + \mathcal{U}$, s is the width of the Gaussian orbital, and $2d$ is the interwell distance. Equation (5) is valid for both negative ($\mathcal{U} \leqslant 0$, attractive) and positive ($\mathcal{U} > 0$, repulsive) values; similarly, the expressions in Eqs. (6)–(8) below are valid in the whole range $-\infty < \mathcal{U} < +\infty$. Note that $\mathcal{Q}(-\mathcal{U}) = \mathcal{P}(\mathcal{U}) \equiv \sqrt{\mathcal{U}^2+16} - \mathcal{U}$ and that $\mathcal{U}\mathcal{P}(\mathcal{U}) \to 8$ when $\mathcal{U} \to \infty$.

In Eq. (5), four specific cos terms contribute, displaying oscillations along the main diagonal ($k_1 - k_2$), the antidiagonal ($k_1 + k_2$), and the two axes (k_1 and k_2). These four terms are supplemented with a constant fifth, circularly symmetric contribution. Each of these terms is damped by an exponential prefactor $e^{-2s^2(k_1^2+k_2^2)}$, whose range ($1/2s^2$) depends on the width s of the displaced Gaussian orbitals. This fact accounts for the different number of visible individual features (circular

humps or fringes) in the CI momentum maps between the top and bottom row of Fig. 1. Indeed, a narrower confining potential (i.e., the one with $\omega = 2\pi \times 15$ kHz) results in a smaller spatial extent of the associated single-particle states compared to a wider confining potential (i.e., the one with $\omega = 2\pi \times 8$ kHz); the oscillator length (and thus s) is inversely proportional to $\sqrt{\omega}$, leading to a damping range $1/2s^2 \propto \omega/2$.

The evolution of the analytic weights for the Hubbard ground state [coefficients in front of the four cos terms plus the constant term in Eq. (5) without the overall common factor $2s^2 e^{-2s^2(k_1^2+k_2^2)}/\pi$] is plotted as a function of U/t in Fig. 2(a); the spectra for the ground and three lowest excited states are displayed in Fig. 2(e). The variation of these weights provides a direct interpretation of the evolution of the CI momentum maps in Fig. 1. In fact, for noninteracting fermions ($g \sim 0$ or $U = 0$), all five terms contribute in a substantial way in the sum of Eq. (5), and this leads to the plaid pattern in Figs. 1(b) and 1(j). For strong g (or high U/t), only two contributions survive, i.e., the constant and the $\cos[2d(k_1 - k_2)]$ terms with equal weights. The corresponding Hubbard momentum map (for $U/t = 8$) plotted in Fig. 2(c) [see lower, green star in Fig. 2(e)] is found to agree with the pattern and orientation of the fringes observed in the CI-calculated maps in Figs. 1(f) and 1(n). The analytic parameter s in Fig. 2(c) was adjusted to correspond to a potential well with a steeper confinement (i.e., $\omega = 2\pi \times 15$ kHz); in this case, there are five visible fringes in Fig. 2(c) precisely as in the CI case in Fig. 1(n). Note that in the strong-interaction case, the two-term $1 + \cos[2d(k_1 - k_2)] = 2\cos^2[d(k_1 - k_2)]$ pattern can be reproduced also using [11] a Heisenberg-Hamiltonian modeling.

IV. ANALYSIS OF EXCITED STATES

CI momentum maps for the first three excited states are displayed in Fig. 3. For the first- (triplet) and second- (singlet) excited states [see the the yellow and blue stars in Fig. 3(a)], the momentum correlation maps are independent of the interparticle interaction (because of the wave-function nodal structure for these excited states), and thus we display for these states the results for a single value of the interaction ($U/t = 8$); see Figs. 3(b) and 3(c), respectively. Indeed, the analytic expressions of the corresponding two-site Hubbard model contain only a single sinusoidal term, independent of the parameter U/t, namely,

$$\mathcal{G}^{S=1,S_z=0}_{\mathrm{Hub,1stex}}(k_1,k_2) \propto \frac{4s^2 e^{-2s^2(k_1^2+k_2^2)} \sin^2[d(k_1 - k_2)]}{\pi}, \quad (6)$$

and

$$\mathcal{G}^{S=0,S_z=0}_{\mathrm{Hub,2ndex}}(k_1,k_2) \propto \frac{4s^2 e^{-2s^2(k_1^2+k_2^2)} \sin^2[d(k_1 + k_2)]}{\pi}. \quad (7)$$

We have checked that Eq. (6) applies to the other two $S = 1$, $S_z = \pm 1$ triplet states as well.

In Fig. 3(b) (first CI excited state), the valley of vanishing values lies along the main diagonal (antibunching behavior), a fact that reflects the Pauli exchange principle which comes into play for a triplet state ($S = 1$, antisymmetric space wave function). We further note that in Fig. 3(c) (second CI excited state), the orientation of the fringes is perpendicular to that in Fig. 3(b), a behavior that reflects the $\sin^2[d(k_1 + k_2)]$ oscillatory pattern in Eq. (7) (associated with the B_3, $S = 0$ symmetric-in-space Bell state) versus the $\sin^2[d(k_1 - k_2)]$ one in Eq. (6).

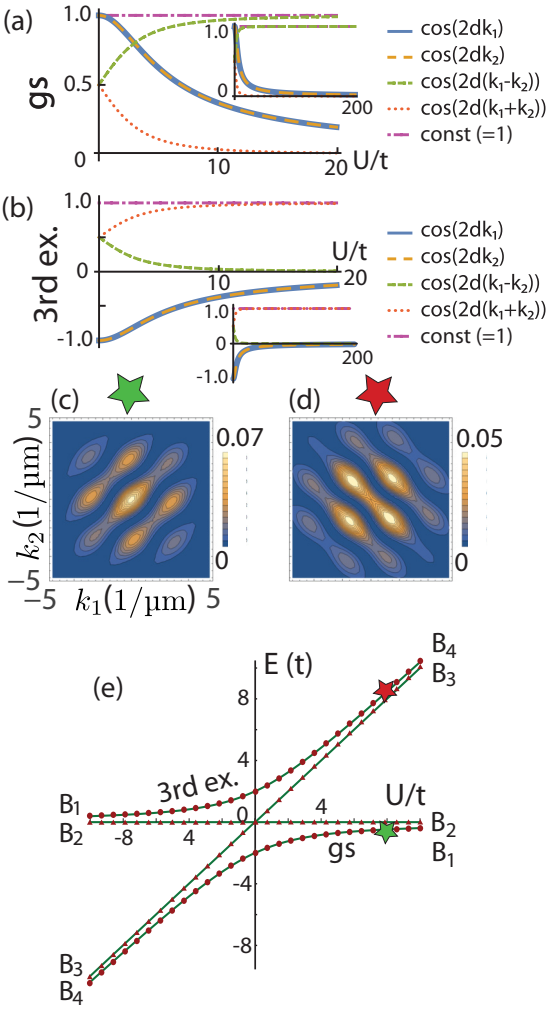

FIG. 2. Plots of analytic weights of the (a) ground and (b) third-excited states [both singlets; see Eqs. (5) and (8)] of the various contributing terms in the two-body momentum correlations as a function of the strength of the Hubbard interaction parameter U/t. The contributions to the various terms in Eqs. (5) and (8) are identified by different colors, as indicated on the right in (a) and (b). (c),(d) The Hubbard momentum maps at $U/t = 8$ for the ground (green star) and third-excited (red star) states. (e) The energy spectrum (solid lines) of the two-site Hubbard model covering both the attractive ($U/t < 0$) and repulsive ($U/t > 0$) ranges. The symbols B_j, $j = 1,\ldots,4$, denote the four Bell states at $U/t \to \pm\infty$. The red dots are the corresponding microscopic CI energies. The Hubbard model in (c)–(e) corresponds to the CI calculation with $2d = 2$ μm and $\omega = 2\pi \times 15$ kHz. Hubbard-model analytic two-particle spatial and momentum correlation maps for the ground state and the three lowest excited states for the repulsive ($U/t = 8$) and attractive ($U/t = -8$) cases are shown in Figs. 6–8. Note the reversal of the energy ordering of the Bell states for the Hubbard $U/t \to -\infty$ and $U/t \to +\infty$ limits.

Figures 3(d)–3(f) describe the evolution with increasing repulsion of the CI momentum maps for the third-excited state [orange stars on the upper curve in Fig. 3(a)]. This evolution

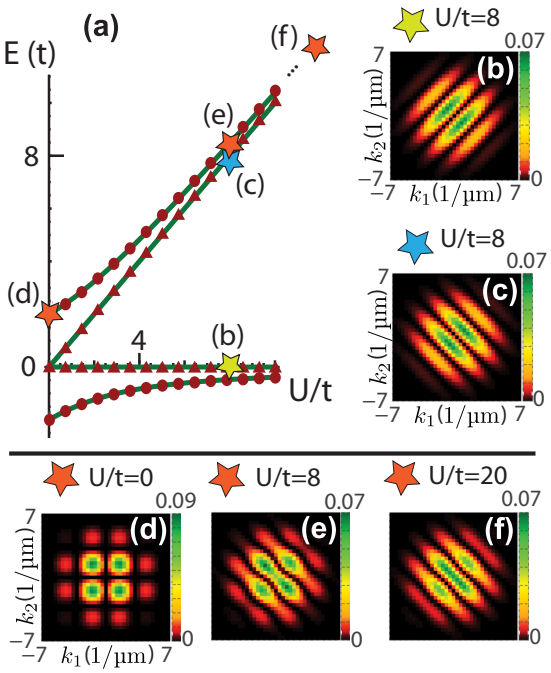

FIG. 3. CI momentum correlation maps for two fermions in a double well associated with the first three excited states, denoted by stars colored as follows: (b) yellow ($U/t = 8$, $g = 4.8 \times 10^{-3}$ in units of $\hbar\omega l_0^2$), (c) blue ($U/t = 8$, $g = 4.8 \times 10^{-3}$), (d) orange ($U/t = 0$, $g = 5.5 \times 10^{-6}$), (e) orange ($U/t = 8$, $g = 4.8 \times 10^{-3}$), and (f) orange ($U/t = 20$, $g = 1.2 \times 10^{-2}$), respectively. The interwell distance is $2d = 2$ μm and the steeper potential confinement ($\omega = 2\pi \times 15$ kHz) is used. The energy spectrum of the corresponding two-site Hubbard model is plotted in (a). The stars in (a) indicate the specific values of U/t (corresponding to particular g's) for which the CI momentum maps for the (b) first-excited, (c) second-excited, and (d)–(f) third-excited states were calculated. The red dots or triangles in (a) are the corresponding microscopic CI energies.

can be interpreted by considering the corresponding analytic two-site Hubbard momentum correlation,

$$\mathcal{G}^{S=0,S_z=0}_{\mathrm{Hub,3rdex}}(k_1,k_2) \propto \frac{2s^2 e^{-2s^2(k_1^2+k_2^2)}}{\pi[16-\mathcal{U}\mathcal{P}(\mathcal{U})]} \times \{[8-\mathcal{U}\mathcal{P}(\mathcal{U})]\cos[2d(k_1-k_2)] + 8\cos[2d(k_1+k_2)] - 4\mathcal{P}(\mathcal{U})\cos(2dk_1) - 4\mathcal{P}(\mathcal{U})\cos(2dk_2) + 16 - \mathcal{U}\mathcal{P}(\mathcal{U})\}, \quad (8)$$

where, as mentioned before, $\mathcal{P}(\mathcal{U}) = \sqrt{\mathcal{U}^2+16} - \mathcal{U}$.

The analytic weights of the five contributing terms in Eq. (8) as a function of U/t are plotted in Fig. 2(b). [As mentioned before, $\mathcal{U}\mathcal{P}(\mathcal{U}) \to 8$ when $\mathcal{U} \to \infty$.] For the noninteracting limit ($U = 0$), all five terms contribute and yield a plaid pattern [see Fig. 3(d)], as was also the case for the singlet ground state. For very strong interactions, only the two contributions $1 + \cos[2d(k_1+k_2)] = 2\cos^2[d(k_1+k_2)]$ survive; see Fig. 3(f) corresponding to $U/t = 20$. For an intermediate $U/t = 8$, Eq. (8) is plotted in Fig. 2(d) [see upper, red star in Fig. 2(e)], exhibiting fringes with a dominant $1 + \cos[2d(k_1+k_2)]$ behavior, which is, however, distorted by residual humps due to the other three weaker terms. The Hubbard pattern in Fig. 2(d) agrees very well with the CI momentum map in Fig. 3(e); for additional two-particle spatial and momentum correlation maps according to the Hubbard model, see Figs. 6–8.

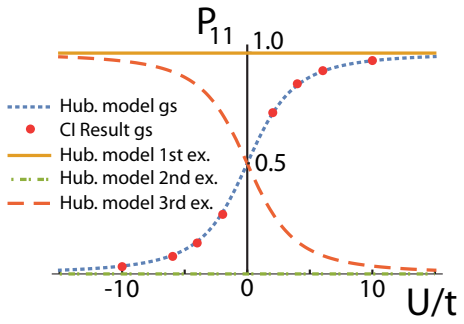

FIG. 4. The probability P_{11}, that is, the so-called coincidence probability—commonly measured in HOM and HOM-like experiments—for finding a particle in one of the wells and another particle in the other well, calculated here as a function of the Hubbard interparticle interaction strength parameter $\mathcal{U} = U/t$. Results are shown for two particles in a double-well trap, with an interwell distance $2d = 2$ μm. Results are shown for attractive ($U < 0$) and repulsive ($U > 0$) interactions, for both the ground state (gs) and three lowest excited (ex.) states. The red dots on the blue (short dashes) curve display the corresponding microscopic (CI) results for the ground state.

V. ENTANGLEMENT ASPECTS AND CONNECTION TO THE HONG-OU-MANDEL INTERFERENCE PHYSICS

The Hubbard-model eigenstates (see details in Appendix D 1) are a superposition of the four maximally entangled Bell states $B_1 = (|LR\rangle - |RL\rangle)/\sqrt{2}$, $B_2 = (|LR\rangle + |RL\rangle)/\sqrt{2}$, $B_3 = (|LL\rangle - |RR\rangle)/\sqrt{2}$, and $B_4 = (|LL\rangle + |RR\rangle)/\sqrt{2}$, where $|L\rangle$ and $|R\rangle$ are, respectively, the single-particle states (including spin) in the left or right well; the superposition coefficients depend on the parameter $\mathcal{U}$. This is illustrated in Fig. 2(e), where the corresponding Bell states at $\mathcal{U} \to \pm\infty$ are explicitly denoted. The first- and second-excited states are the pure Bell states B_2 and B_3, respectively, for any $\mathcal{U}$. The Hong-Ou-Mandel [15] interference phenomena are related to the coincidence probability P_{11} of having two particles in the B_3 (spin-up and spin-down fermions mimicking indistinguishable bosons [3,19], $P_{11} = 0$) or B_2 state (indistinguishable fermions [17,18], $P_{11} = 1$ due to the Pauli exclusion principle); see Fig. 4. The state B_4, being also an entangled NOON state [22], can provide a further analogy to the bosonic HOM effect. Finally, the state B_1 can also be related to the fermionic HOM effect; however, in the context of the ground state of the Hubbard dimer, this state is associated with the process of fermionization [12,23] due to large interatomic repulsion, rather than with a quantum-statistics effect.

In our treatment, P_{11} can be related to the second-order spatial and momentum correlations through the diagonal elements of the two-particle density matrix ρ_{ijkl} which decomposes the second-order correlation maps to left-right (L,R) components. From the momentum correlation maps and using the Hubbard

modeling for simplicity, one has

$$\mathcal{G}_{\rm Hub}(k_1,k_2) = \sum_{i,j,k,l=L,R} \eta_{ijkl}^{\rm Hub,2nd}(k_1,k_2)$$
$$= \sum_{i,j,k,l=L,R} \rho_{ijkl}^{\rm Hub,2nd} \psi_{i\uparrow}(k_1)\psi_{j\downarrow}(k_2)$$
$$\times \psi_{k\uparrow}^{\dagger}(k_1)\psi_{l\downarrow}^{\dagger}(k_2). \quad (9)$$

The explicit expressions for ρ_{ijkl} for the four Hubbard states are given in Appendices D 3–D 6. $P_{11} = \rho_{LRLR} + \rho_{RLRL}$; Fig. 4 displays the dependence of P_{11} on $\mathcal{U}$.

Additional HOM [and also Handbury-Brown-Twiss [1,2,24,25] (HBT)] aspects can be evoked based on the role played by the four Bell states in our approach. Developing corresponding experimental protocols that will test, among other possibilities, the interplay of beam splitters and interaction effects is beyond the scope of this paper. However, we mention here two possible paths. The first is the measurement of spatial noise [26] in the particle counts in the image of the expanding cloud of the two ultracold atoms; this image reflects in space the momentum correlation maps. Such measurements along the main diagonal or antidiagonal of the image will correspond to the observation of both HOM antibunching and bunching types with fermions when using the first- or second-excited states, respectively; see Figs. 3(b) and 3(c). This will follow the spirit of Refs. [17,18] that address the fermionic case for electrons by measuring current noise in mesoscopic semiconductors [27]. Away from the two diagonals, the noise measurements may be associated with oscillatory HBT interference reflecting the distance $2d$ between the two wells [1,2,24,25]. Furthermore, if the left- or right-well provenance of the particles can be determined, noise measurements associated with the components η_{ijkl} of the momentum correlation maps [see Eq. (9)] could be performed, yielding additional pathways for exploration of particle interference effects. The second path relates to entanglement aspects by using the density matrix ρ_{ijkl} in the spirit of Refs. [6,9].

VI. SUMMARY

In conclusion, with the use of a two-particle density matrix constructed via configuration-interaction exact diagonalization of the microscopic Hamiltonian, we have explored the systematic evolution of characteristic, damped interference patterns in the two-particle momentum and spatial correlation maps of two ultracold fermionic atoms trapped in a double-well potential, over the entire range of variation of the contact (both repulsive and attractive) interatomic interaction strength. For the singlet ground state, the two-body momentum maps were found to transform from a square-plaid pattern [Figs. 1(b) and 1(j)] for vanishing interparticle interaction to a system of striped interference fringes oriented in the direction parallel to the main diagonal of the square two-particle map [Figs. 1(h) and 1(p)]. The most intense fringe lies along the main diagonal, indicating bunching. Our theoretical results (Fig. 1, top row) agree well with the evolution (found with increasing strength) of preparatory experimentally measured [7] momentum correlation maps [28]. We have also analyzed two-body momentum correlation maps for low-lying excited states (Figs. 2 and 3). The triplet-excited state is associated with antibunching [see Fig. 3(b)]. A derived modified-Hubbard-type effective model, incorporating spatial degrees of freedom (i.e., interwell distance and particle localization length) in addition to the customary on-site U and hopping (t) Hubbard-Hamiltonian parameters (determined in each case from the CI results), has been found to reproduce well the microscopic CI results. Importantly, this development allowed us to uncover analytic expressions capturing the full evolution of the two-particle momentum correlation maps over the entire range of interparticle interactions—from the noninteracting regime ($U/t = 0$, with substantial ground-state site-double-occupancy contributions) to the Mott-insulating regime with large U/t.

ACKNOWLEDGMENTS

This work has been supported by a grant from the Air Force Office of Scientific Research (USA) under Award No. FA9550-15-1-0519. Calculations were carried out at the GATECH Center for Computational Materials Science.

APPENDIX A: DERIVATION OF ANALYTIC HUBBARD-TYPE INTERFERENCE FORMULAS FOR TWO PARTICLES

Here we illustrate in detail the derivation of the analytic interference formulas for $N = 2$ particles, allowing a rather immediate generalization to more complex cases with $N > 2$ particles. For this analytic modeling, we assume that the spatial part of the orbital of the jth particle is approximated by a displaced Gaussian function (localized at a position d_j),

$$\psi_j(x) = \frac{1}{(2\pi)^{1/4}\sqrt{s}} \exp\left[-\frac{(x-d_j)^2}{4s^2}\right], \quad (A1)$$

where s denotes the width of the Gaussian functions. The single-particle orbital $\psi_j(k)$ in the momentum Hilbert space is given by the Fourier transform of $\psi_j(x)$, namely, $\psi_j(k) = (1/\sqrt{2\pi})\int_{-\infty}^{\infty}\psi_j(x)\exp(ikx)dx$. Performing this Fourier transform, one finds

$$\psi_j(k) = \frac{2^{1/4}\sqrt{s}}{\pi^{1/4}} \exp(-k^2s^2)\exp(id_jk). \quad (A2)$$

In our previous paper [11], we focused on well-localized particles within each well (neglecting the possibility of double occupancy in each well), a condition that is satisfied for strong repulsion. Here we are interested in an analytical model for all interaction strengths, allowing for double occupancy. We therefore consider the more general case of the two-site Hubbard model instead of the Heisenberg model (as was done in Ref. [11]). The two particles are localized at two different wells, at positions $d_1 < 0$ and $d_2 > 0$, which together with the spin yields four possible spin eigenfunctions $|\circ,\uparrow\downarrow\rangle$, $|\downarrow,\uparrow\rangle$, $|\uparrow,\downarrow\rangle$, and $|\uparrow\downarrow,\circ\rangle$. These spin eigenfunctions form a complete many-body base for the diagonalization of the fermionic Hubbard Hamiltonian,

$$H = -\sum_{\sigma}(\hat{c}_{1,\sigma}^{\dagger}\hat{c}_{2,\sigma} + \hat{c}_{2,\sigma}^{\dagger}\hat{c}_{1,\sigma}) + \mathcal{U}\sum_{i=1}^{2}\hat{n}_{i\uparrow}\hat{n}_{i\downarrow}, \quad (A3)$$

where σ sums over the up ($\uparrow$) and down ($\downarrow$) spins. The ratio $\mathcal{U} = U/t$, where U and t are the on-site repulsion and the nearest-neighbor hopping parameters. The energies are expressed in units of t.

There are many equivalent ways of writing the Hubbard-model basis in the second-quantization formalism, and throughout this paper we use the following convention:

$$b_1 = \hat{c}^\dagger_{2\uparrow}\hat{c}^\dagger_{2\downarrow}|\rangle = |RR\rangle = |\circ,\uparrow\downarrow\rangle, \tag{A4}$$

$$b_2 = \hat{c}^\dagger_{1\downarrow}\hat{c}^\dagger_{2\uparrow}|\rangle = |RL\rangle = |\downarrow,\uparrow\rangle, \tag{A5}$$

$$b_3 = \hat{c}^\dagger_{1\uparrow}\hat{c}^\dagger_{2\downarrow}|\rangle = |LR\rangle = |\uparrow,\downarrow\rangle, \tag{A6}$$

$$b_4 = \hat{c}^\dagger_{1\uparrow}\hat{c}^\dagger_{1\downarrow}|\rangle = |LL\rangle = |\uparrow\downarrow,\circ\rangle. \tag{A7}$$

In the third column above, the spin of the particle is not denoted explicitly. In this case, the following mnemonic rule is helpful: the spin-up particle is always written first inside the ket $|\cdots\rangle$.

For a small number of particles, the Hubbard Hamiltonian can be exactly diagonalized (for instance, using SNEG [29]). For $S_z = 0$, a general solution of the two-site Hubbard Hamiltonian using the aforementioned second-quantization basis is of the form

$$\Phi = a(\mathcal{U})|\circ,\uparrow\downarrow\rangle + b(\mathcal{U})|\downarrow,\uparrow\rangle + c(\mathcal{U})|\uparrow,\downarrow\rangle + d(\mathcal{U})|\uparrow\downarrow,\circ\rangle. \tag{A8}$$

The coefficients $a(\mathcal{U}),\ldots,d(\mathcal{U})$ of course satisfy the constraint that Φ is normalized. Naturally, such a Hubbard-model solution yields the wave function in second-quantization form. Our modification aims at including the spatial component of the wave function by associating each basis ket $b_i, i = 1,\ldots,4$, with a determinant of spin orbitals $\psi_{j,\sigma}(x) = \psi_j(x)\sigma$, where σ represents the spin. When the spin orbitals are localized on the left or right well, they will also be denoted as $|L\rangle$ or $|R\rangle$, respectively. The corresponding determinants $\mathcal{D}$ to each basis ket are (the tilde indicates the incorporation of the space orbitals)

$$|\widetilde{RR}\rangle = \mathcal{D}_{|\circ,\uparrow\downarrow\rangle}(x_1,x_2) = \frac{1}{\sqrt{2!}}[\psi_{2\uparrow}(x_1)\psi_{2\downarrow}(x_2) - \psi_{2\uparrow}(x_2)\psi_{2\downarrow}(x_1)], \tag{A9}$$

$$|\widetilde{RL}\rangle = \mathcal{D}_{|\downarrow,\uparrow\rangle}(x_1,x_2) = \frac{1}{\sqrt{2!}}[\psi_{1\downarrow}(x_1)\psi_{2\uparrow}(x_2) - \psi_{1\downarrow}(x_2)\psi_{2\uparrow}(x_1)], \tag{A10}$$

$$|\widetilde{LR}\rangle = \mathcal{D}_{|\uparrow,\downarrow\rangle}(x_1,x_2) = \frac{1}{\sqrt{2!}}[\psi_{1\uparrow}(x_1)\psi_{2\downarrow}(x_2) - \psi_{1\uparrow}(x_2)\psi_{2\downarrow}(x_1)], \tag{A11}$$

$$|\widetilde{LL}\rangle = \mathcal{D}_{|\uparrow\downarrow,\circ\rangle}(x_1,x_2) = \frac{1}{\sqrt{2!}}[\psi_{1\uparrow}(x_1)\psi_{1\downarrow}(x_2) - \psi_{1\uparrow}(x_2)\psi_{1\downarrow}(x_1)]. \tag{A12}$$

We can therefore write the full wave function, including the space and spin parts, as

$$\Phi(x_1,x_2) = a(\mathcal{U})\mathcal{D}_{|\circ,\uparrow\downarrow\rangle}(x_1,x_2) + b(\mathcal{U})\mathcal{D}_{|\downarrow,\uparrow\rangle}(x_1,x_2) + c(\mathcal{U})\mathcal{D}_{|\uparrow,\downarrow\rangle}(x_1,x_2) + d(\mathcal{U})\mathcal{D}_{|\uparrow\downarrow,\circ\rangle}(x_1,x_2), \tag{A13}$$

where the coefficients are, in general, dependent on the inter-well distance $2d = d_2 - d_1$ ($d_1 < d_2$) and the width s.

We can now use the wave function $\Phi(x_1,x_2)$, together with the formulas described in the main paper [see Eqs. (3) and (4) therein], to obtain the two-particle correlation expressions in real and momentum space [see Eqs. (5)–(8)]. The integrations associated with the Fourier transforms can be carried out with the help of the MATHEMATICA algebraic computer language [30].

APPENDIX B: EXTRACTION OF HUBBARD-MODEL PARAMETERS FROM THE CI CALCULATION

In order to compare our analytical model with the CI results, it is important to relate the interparticle interaction strength g [see Eq. (2)] with the Hubbard parameter U, and to extract the value of the hopping parameter t from the single-particle energy spectrum associated with the external confining potential. Given the single-particle spectrum, the value of t can be extracted as $t = (e_2 - e_1)/2$, where e_1 and e_2 are the ground and first-excited single-particle energies, respectively. This can be directly inferred from the tight-binding limit (setting $U = 0$).

In order to determine U from the CI, we first take a close look at the Hubbard-model energy levels and their properties. An exact diagonalization of the Hubbard Hamiltonian shows that the second-excited-state energy $E_3(U)$ is directly proportional to U with $E_3(U) = U + 2t + E_1(0)$, where $E_1(0)$ is the noninteracting ground-state energy. For noninteracting ($U = 0$) particles, the energy of the second-excited state is therefore simply given as $E_3(0) = 2t + E_1(0)$. Consequently, one can extract the parameter U directly from the difference between the noninteracting and interacting second-excited-state energy, $U = E_3(U) - E_3(0)$. This is a trivial result within the Hubbard model, but it also applies for our CI calculations.

In order to verify that U can be determined by using the corresponding energy difference from our CI spectrum, i.e., $U = E_3^{\mathrm{CI}}(g) - E_3^{\mathrm{CI}}(0)$, we look at the properties of the second-excited CI state. In the Hubbard model, the second-excited state is given as $(|LL\rangle - |RR\rangle)/\sqrt{2}$, containing only doubly occupied sites (as we would expect since U represents the on-site interaction energy). It is easily verified via conditional probability distributions (CPDs) [14,20,31,32] in which, in analogy with the Hubbard-model case, the second-excited CI state consists solely of doubly occupied wells; see Fig. 5. We therefore proceed to determine U using $U = E_3^{\mathrm{CI}}(g) - E_3^{\mathrm{CI}}(0)$. Afterwards, we compare the CI and Hubbard energy levels using values for U obtained from the CI in this way and find very good agreement between the CI spectrum and the Hubbard model spectrum [see Figs. 2(e) and 3(a)], validating our approach for extracting U from the CI calculation.

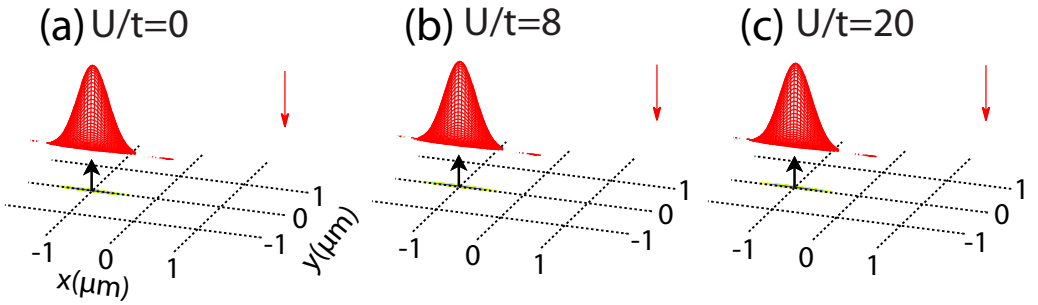

FIG. 5. This figure shows spin-resolved conditional probability densities (SR-CPDs) for two particles in the second-excited state in a double well. We plot the SR-CPD for three different interaction strengths: (a) $g = 5.5\ 10^{-6}\hbar\omega l_0^2$ (corresponding to $U/t = 0$), (b) $g = 4.8\ 10^{-3}\hbar\omega l_0^2$ (corresponding to $U/t = 8$), and (c) $g = 1.2\ 10^{-2}\hbar\omega l_0^2$ (corresponding to $U/t = 20$). The black up-arrow represents the fixed position of the spin-up particle in the plane of the grid. The red down-arrow indicates that we are calculating the resulting occupation probability (density) for a spin-down particle; see the plotted red surface. As is apparent from the figure, the red probability surface is directly situated on top of the black (spin-up) fixed point for all interaction strengths. This indicates strong double occupancy. The second well of the double well at $d_2 = d = 1\ \mu$m is practically unoccupied. This double occupancy is what allows us to extract the Hubbard on-site interaction parameter U from the energy level of the second-excited CI state. The parameters for the double wells are $\omega = \omega_x = 2\pi \times 15$ kHz, $\omega_y = 2\pi \times 1500$ kHz, and $\epsilon_b = 0.5$ (interwell barrier $V_b/h = 33.5$ kHz). The interwell distance is $2d = 2\ \mu$m.

APPENDIX C: ADDITIONAL FIGURES PORTRAYING HUBBARD-MODEL TWO-PARTICLE MOMENTUM CORRELATION MAPS

In order to further highlight the extent to which our modified-solutions Hubbard model reproduces the microscopic CI two-particle space and momentum correlations, we display three additional figures, Figs. 6–8. Both space and momentum correlation maps in Fig. 6 should be compared with the corresponding CI ones in the bottom row (steeper confinement with $\omega = 2\pi \times 15$ kHz) of Fig. 1. The momentum correlation maps in Fig. 7 for the repulsive case with $U/t = 8$ should be compared with those CI ones in Figs. 3(b), 3(c) and 3(e) [due to the contrast, the outer fringes in Figs. 3(b) and 3(c) are better seen after one enlarges these figure panels]. The corresponding results for the attractive case with $U/t = -8$ are shown for completeness in Fig. 8.

APPENDIX D: THE SECOND-ORDER (TWO-BODY) DENSITY MATRICES DERIVED IN THE HILBERT SPACE OF THE MODIFIED-SOLUTIONS HUBBARD MODEL AND THEIR RELATION TO THE CORRELATION MAPS

1. Solution of the two-site two-particle Hubbard model

Here we outline the solution of the two-site Hubbard model with two spin-1/2 fermions. The Hubbard Hamiltonian in second quantization is given in Eq. (A3). We remind the reader that U in Eq. (A3) is the on-site interaction, t is the tunneling parameter, and $\hat{n}_{i\sigma}$ is the number operator at site i for spin σ. For convenience, we repeat our definition of the Hubbard-model basis functions [see Eqs. (A4)–(A7)]:

$$b_1 = \hat{c}^\dagger_{2\uparrow}\hat{c}^\dagger_{2\downarrow}|\rangle = |RR\rangle = |\circ,\uparrow\downarrow\rangle, \tag{D1}$$

$$b_2 = \hat{c}^\dagger_{1\downarrow}\hat{c}^\dagger_{2\uparrow}|\rangle = |RL\rangle = |\downarrow,\uparrow\rangle, \tag{D2}$$

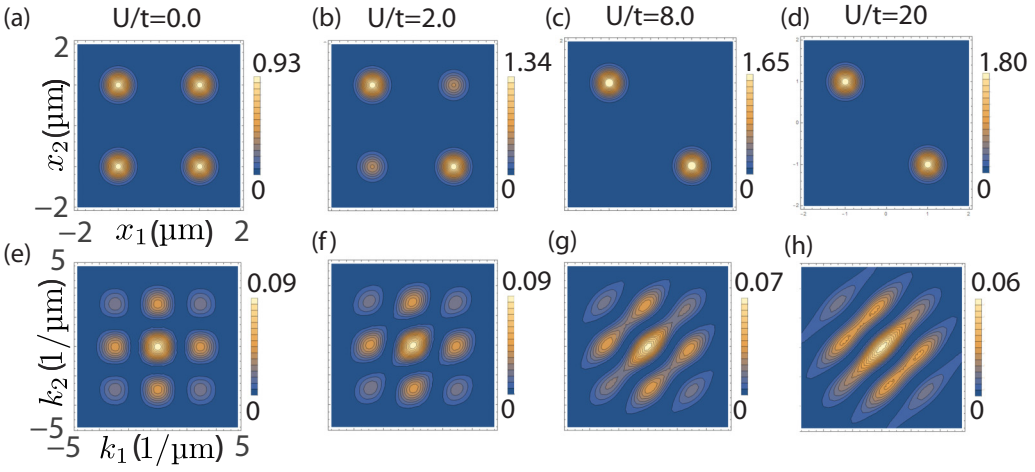

FIG. 6. The analytic Hubbard-model ground-state (singlet) (a)–(d) space and (e)–(h) momentum [see Eq. (5)] two-particle correlation maps for two ultracold fermions in a double well, as a function of the Hubbard interaction strength U/t. The interwell distance is $2d = 2\ \mu$m and the width of the displaced Gaussian functions is $s = 0.2\ \mu$m.

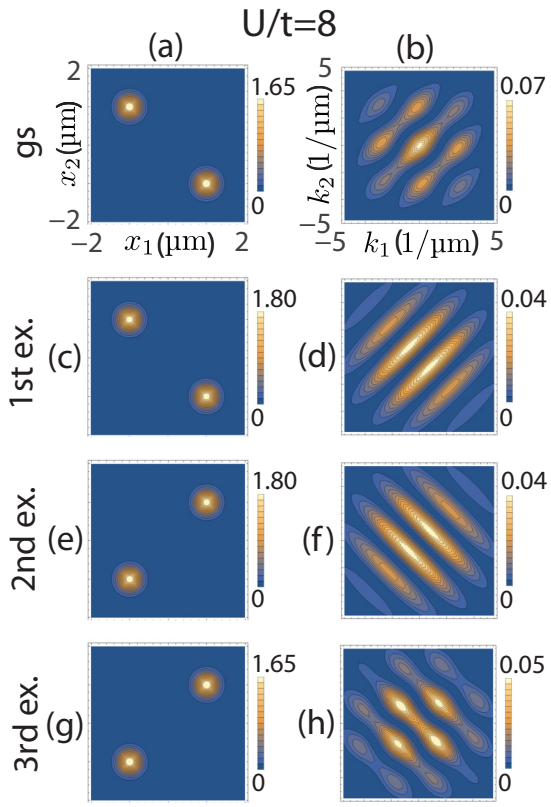

FIG. 7. Hubbard-model analytic two-particle correlation maps for the ground state and the three lowest excited states (as marked in the figure) of two ultracold fermions in a double well, calculated for an intermediate *positive* value of the Hubbard interaction strength $U/t = 8$. (a),(c),(e),(g) Two-particle spatial correlations maps. (b),(d),(f),(h) Two-particle momentum correlation maps according to Eqs. (5)–(8). The interwell distance is $2d = 2$ μm and the width of the displaced Gaussian functions is $s = 0.2$ μm.

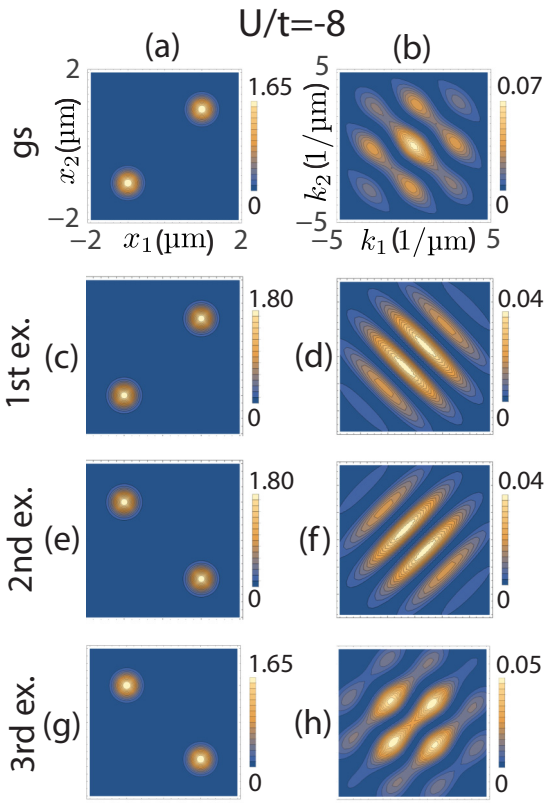

FIG. 8. Hubbard-model analytic two-particle correlation maps for the ground state and the three lowest excited states (as marked in the figure) of two ultracold fermions in a double well, calculated for an intermediate *negative* value of the Hubbard interaction strength $U/t = -8$. (a),(c),(e),(g) Two-particle spatial correlations maps. (b),(d),(f),(h) Two-particle momentum correlation maps according to Eqs. (5)–(8). The interwell distance is $2d = 2$ μm and the width of the displaced Gaussian functions is $s = 0.2$ μm.

$$b_3 = \hat{c}^\dagger_{1\uparrow}\hat{c}^\dagger_{2\downarrow}|\rangle = |LR\rangle = |\uparrow,\downarrow\rangle, \tag{D3}$$

$$b_4 = \hat{c}^\dagger_{1\uparrow}\hat{c}^\dagger_{1\downarrow}|\rangle = |LL\rangle = |\uparrow\downarrow,\circ\rangle, \tag{D4}$$

where L and R represent site 1 and 2, respectively. There are many equivalent notations for these basis functions in the literature and we have listed three of them in Eqs. (D1)–(D4). In the following, we will use the L,R notation. The basis set in Eqs. (D1)–(D4) spans the Hilbert space of the two-site two-particle Hubbard model and the resulting Hubbard matrix is

$$\mathscr{H} = \begin{bmatrix} U & t & -t & 0 \\ t & 0 & 0 & t \\ -t & 0 & 0 & -t \\ 0 & t & -t & U \end{bmatrix}. \tag{D5}$$

Diagonalization of this Hamiltonian yields the following eigenenergies:

$$E_1 = \frac{1}{2}(U - \sqrt{16t^2 + U^2}), \tag{D6}$$

$$E_2 = 0, \tag{D7}$$

$$E_3 = U, \tag{D8}$$

$$E_4 = \frac{1}{2}(U + \sqrt{16t^2 + U^2}). \tag{D9}$$

The eigenfunctions corresponding to these eigenvalues are

$$\begin{aligned}\Phi_1 &= A(U,t)|RR\rangle + B(U,t)|RL\rangle - B(U,t)|LR\rangle \\ &\quad + A(U,t)|LL\rangle \\ &= A(U,t)(|RR\rangle + |LL\rangle) + B(U,t)(|RL\rangle - |LR\rangle) \\ &= A(U,t)\sqrt{2}|B_4\rangle - B(U,t)\sqrt{2}|B_1\rangle,\end{aligned} \tag{D10}$$

$$\Phi_2 = \frac{1}{\sqrt{2}}(|RL\rangle + |LR\rangle) = |B_2\rangle, \tag{D11}$$

$$\Phi_3 = \frac{1}{\sqrt{2}}(|LL\rangle - |RR\rangle) = |B_3\rangle, \tag{D12}$$

$$\begin{aligned}\Phi_4 &= C(U,t)|RR\rangle + D(U,t)|RL\rangle - D(U,t)|LR\rangle \\ &\quad + C(U,t)|LL\rangle \\ &= C(U,t)(|RR\rangle + |LL\rangle) + D(U,t)(|RL\rangle - |LR\rangle) \\ &= C(U,t)\sqrt{2}|B_4\rangle - D(U,t)\sqrt{2}|B_1\rangle,\end{aligned} \tag{D13}$$

where

$$A(U,t) = 1\Big/\sqrt{\frac{(\sqrt{16t^2+U^2}+U)^2}{8t^2}+2}, \tag{D14}$$

$$B(U,t) = -\frac{\sqrt{16t^2+U^2}+U}{4t}\Big/\sqrt{\frac{(\sqrt{16t^2+U^2}+U)^2}{8t^2}+2}, \tag{D15}$$

$$C(U,t) = 1\Big/\sqrt{\frac{(U-\sqrt{16t^2+U^2})^2}{8t^2}+2}, \tag{D16}$$

$$D(U,t) = \frac{-U+\sqrt{16t^2+U^2}}{4t}\Big/\sqrt{\frac{(U-\sqrt{16t^2+U^2})^2}{8t^2}+2}, \tag{D17}$$

and $|B_1\rangle,|B_2\rangle,|B_3\rangle,|B_4\rangle$ are the four Bell states:

$$|B_1\rangle = \frac{1}{\sqrt{2}}(|LR\rangle - |RL\rangle), \tag{D18}$$

$$|B_2\rangle = \frac{1}{\sqrt{2}}(|LR\rangle + |RL\rangle), \tag{D19}$$

$$|B_3\rangle = \frac{1}{\sqrt{2}}(|LL\rangle - |RR\rangle), \tag{D20}$$

$$|B_4\rangle = \frac{1}{\sqrt{2}}(|LL\rangle + |RR\rangle). \tag{D21}$$

Writing the Hubbard-model solutions in this form has the advantage that it reveals the simple structure of the Hubbard Hamiltonian in the four Bell-states basis, i.e.,

$$\mathscr{H} = \begin{bmatrix} 0 & 0 & 0 & -2t \\ 0 & 0 & 0 & 0 \\ 0 & 0 & U & 0 \\ -2t & 0 & 0 & U \end{bmatrix}. \tag{D22}$$

We note that for two fermions, one can form two additional Bell states by adding and subtracting the $S=1$, $S_z=1$ ($|\uparrow,\uparrow\rangle$) and $S=1$, $S_z=-1$ ($|\downarrow,\downarrow\rangle$) triplet states [33,34]. These two Bell states, however, do not conserve the total spin and thus they are not CI eigenstates.

2. Calculation of the second-order two-body density matrix

For each state of the Hubbard model ($\Phi_1,\Phi_2,\Phi_3,\Phi_4$, denoted in general as Φ), one can obtain the second-order density matrix as $\rho_{\rm Hub}^{S,S_z} = |\Phi\rangle\langle\Phi|$, which can be written in the L, R basis as

$$\rho_{\rm Hub}^{S,S_z} = \sum_{i,j,k,l=L,R} \rho_{ijkl}^{{\rm Hub},S,S_z} |i\ j\rangle\langle k\ l|. \tag{D23}$$

In order to obtain the spatial second-order density matrix (and, subsequently, the second-order spatial correlation function) from the Hubbard-model density matrix, we define an operator that associates single-particle spatial wave functions [ψ; see, e.g., Eq. (A1)] with the L,R basis, as

$$\mathcal{O}_s = \sum_{i,j,k,l=L,R} \psi_{i\uparrow}(x_1)\psi_{j\downarrow}(x_2)\psi^\dagger_{k\uparrow}(x'_1)\psi^\dagger_{l\downarrow}(x'_2)\hat{c}_{1\uparrow}\hat{c}_{2\downarrow}\hat{c}^\dagger_{1\uparrow}\hat{c}^\dagger_{2\downarrow}. \tag{D24}$$

The spatial second-order density matrix can then be obtained as the expectation value of this operator,

$$\mathcal{G}_{\rm Hub}^{S,S_z}(x_1,x_2,x'_1,x'_2) = \langle\Phi|\mathcal{O}_s|\Phi\rangle = {\rm Tr}\left[\rho_{\rm Hub}^{S,S_z}\ \mathcal{O}_s\right], \tag{D25}$$

which yields

$$\mathcal{G}_{\rm Hub}^{S,S_z}(x_1,x_2,x'_1,x'_2) = \sum_{i,j,k,l=L,R} \rho_{ijkl}^{{\rm Hub},S,S_z}\psi_{i\uparrow}(x_1)\psi_{j\downarrow}(x_2)\psi^\dagger_{k\uparrow}(x'_1)\psi^\dagger_{l\downarrow}(x'_2). \tag{D26}$$

The second-order momentum density matrix is obtained through Fourier transform,

$$\begin{aligned}\mathcal{G}_{\rm Hub}^{S,S_z}(k_1,k_2,k'_1,k'_2) &= \frac{1}{4\pi^2}\int_{-\infty}^{\infty} e^{-k_1x_1}dx_1\int_{-\infty}^{\infty} e^{-k_2x_2}dx_2\int_{-\infty}^{\infty} e^{k'_1x'_1}dx'_1 \\ &\times \int_{-\infty}^{\infty} e^{k'_2x'_2}dx'_2 \\ &\times \sum_{i,j,k,l=L,R} \rho_{ijkl}^{{\rm Hub},S,S_z}\psi_i(x_1)\psi_j(x_2)\psi^\dagger_k(x'_1)\psi^\dagger_l(x'_2) \\ &= \sum_{i,j,k,l=L,R} \rho_{ijkl}^{{\rm Hub},S,S_z}\psi_{i\uparrow}(k_1)\psi_{j\downarrow}(k_2)\psi^\dagger_{k\uparrow}(k'_1)\psi^\dagger_{l\downarrow}(k'_2). \end{aligned}\tag{D27}$$

To proceed, we use single-particle Gaussian wave functions for the left and right wells, where L,R indicate that the real-space Gaussian wave function (ψ) is localized in the left (ψ_L) and right (ψ_R) well, respectively. The real-space displaced Gaussian function was given in Eq. (A1); ($d_j<0$ corresponds to L, $d_j>0$ corresponds to R) s is the Gaussian width. Its Fourier transform was given in Eq. (A2).

Using these Gaussian single-particle wave functions, the second-order momentum density-matrix elements can be calculated explicitly,

$$\begin{aligned}\eta_{ijkl}^{{\rm Hub},S,S_z}(k_1,k_2,k'_1,k'_2) &= \rho_{ijkl}^{{\rm Hub},S,S_z}\psi_{i\uparrow}(k_1)\psi_{j\downarrow}(k_2)\psi^\dagger_{k\uparrow}(k'_1)\psi^\dagger_{l\downarrow}(k'_2). \end{aligned}\tag{D28}$$

This allows us to write the second-order momentum density matrix as

$$\mathcal{G}_{\rm Hub}^{S,S_z}(k_1,k_2,k'_1,k'_2) = \sum_{i,j,k,l=L,R} \eta_{ijkl}^{{\rm Hub},S,S_z}(k_1,k_2,k'_1,k'_2). \tag{D29}$$

For a physical interpretation and for the creation of the second-order momentum correlation maps, we are interested only in the diagonal elements of the second-order momentum density matrix, which are given as

$$\mathcal{G}_{\rm Hub}^{S,S_z}(k_1,k_2) = \sum_{i,j,k,l=L,R} \eta_{ijkl}^{{\rm Hub},S,S_z}(k_1,k_2), \tag{D30}$$

with

$$\mathcal{G}_{\rm Hub}^{S,S_z}(k_1,k_2) \equiv \mathcal{G}_{\rm Hub}^{S,S_z}(k_1,k_2,k_1,k_2), \tag{D31}$$

$$\eta_{ijkl}^{{\rm Hub},S,S_z}(k_1,k_2) \equiv \eta_{ijkl}^{{\rm Hub},S,S_z}(k_1,k_2,k_1,k_2). \tag{D32}$$

When evaluating this expression, one needs to account for the orthogonality of the spins. The function $\mathcal{G}_{\rm Hub}^{S,S_z}(k_1,k_2)$ is

termed the second-order (two-body) momentum correlation function. One can obtain the spin-resolved version by only selecting terms with a certain spin configuration. Alternatively, the spin-unresolved version can be obtained by taking all the spin terms into account. In the special case of a two-particle second-order correlation function, both the spin-resolved and the spin-unresolved versions are identical (for a given spin projection) apart from an overall factor. Expressing $\mathcal{G}_{\rm Hub}^{S,S_z}(k_1,k_2)$ using the $\eta_{ijkl}^{{\rm Hub},S,S_z}(k_1,k_2)$ elements has the advantage that the $\eta_{ijkl}^{{\rm Hub},S,S_z}(k_1,k_2)$ clearly show the interference terms that correspond to the individual entries in the Hubbard-model density matrix $\rho_{\rm Hub}^{S,S_z}$. These elements can be read off directly from the matrices given in Appendices D 3–D 6.

3. Ground state

Using $\mathcal{U}=U/t$ and $\mathcal{Q}(\mathcal{U})=\sqrt{16+\mathcal{U}^2}+\mathcal{U}$, the Hubbard-model two-body density matrix is given by

$$\rho_{\rm Hub}^{S=0,S_z=0}=\frac{1}{\mathcal{Q}(\mathcal{U})\mathcal{U}+16}\begin{array}{c}\begin{array}{cccc}LL & LR & RL & RR\end{array}\\ \begin{pmatrix} 4 & \mathcal{Q}(\mathcal{U}) & \mathcal{Q}(\mathcal{U}) & 4 \\ & \frac{\mathcal{Q}(\mathcal{U})\mathcal{U}}{2}+4 & \frac{\mathcal{Q}(\mathcal{U})\mathcal{U}}{2}+4 & \mathcal{Q}(\mathcal{U}) \\ & {\rm H.c.} & \frac{\mathcal{Q}(\mathcal{U})\mathcal{U}}{2}+4 & \mathcal{Q}(\mathcal{U}) \\ & & & 4 \end{pmatrix}\begin{array}{c}LL\\LR\\RL\\RR\end{array}\end{array} \tag{D33}$$

$$=\begin{array}{c}\begin{array}{cccc}LL & LR & RL & RR\end{array}\\ \begin{pmatrix} A(\mathcal{U})^2 & -A(\mathcal{U})B(\mathcal{U}) & -A(\mathcal{U})B(\mathcal{U}) & A(\mathcal{U})^2 \\ & B(\mathcal{U})^2 & B(\mathcal{U})^2 & -A(\mathcal{U})B(\mathcal{U}) \\ & {\rm H.c.} & B(\mathcal{U})^2 & -A(\mathcal{U})B(\mathcal{U}) \\ & & & A(\mathcal{U})^2 \end{pmatrix}\begin{array}{c}LL\\LR\\RL\\RR\end{array}\end{array}. \tag{D34}$$

Note that $\rho_{\rm Hub}^{S=0,S_z=0}$ for the ground state as well as for the excited states (see Appendices D 4–D 6 below) are idempotent. Including the Fourier-transformed wave functions, we obtain

$$\eta_{\rm Hub}^{S=0,S_z=0}(k_1,k_2)=\frac{2s^2e^{-2s^2(k_1^2+k_2^2)}}{\pi[\mathcal{Q}(\mathcal{U})\mathcal{U}+16]}\begin{array}{c}\begin{array}{cccc}LL & LR & RL & RR\end{array}\\ \begin{pmatrix} 4 & e^{-2idk_2}\mathcal{Q}(\mathcal{U}) & e^{-2idk_1}\mathcal{Q}(\mathcal{U}) & 4e^{-2id(k_1+k_2)} \\ & \frac{\mathcal{Q}(\mathcal{U})\mathcal{U}}{2}+4 & \frac{1}{2}e^{-2id(k_1-k_2)}[\mathcal{Q}(\mathcal{U})\mathcal{U}+8] & e^{-2idk_1}\mathcal{Q}(\mathcal{U}) \\ & {\rm H.c.} & \frac{\mathcal{Q}(\mathcal{U})\mathcal{U}}{2}+4 & e^{-2idk_2}\mathcal{Q}(\mathcal{U}) \\ & & & 4 \end{pmatrix}\begin{array}{c}LL\\LR\\RL\\RR\end{array}\end{array}. \tag{D35}$$

Using Eq. (D30) and the second-order momentum matrix in Eq. (D35), one can obtain the two-body ground-state momentum correlation function [see Eq. (5)]. Similarly, the two-body momentum correlation functions for the excited states [see Eqs. (6)–(8)] can be obtained through the use of the matrices given in Appendices D 4–D 6 below.

4. First-excited state

$\rho_{\rm Hub}^{S=1,S_z=0}$ and $\eta_{\rm Hub}^{S=1,S_z=0}(k_1,k_2)$ for the first-excited state of the Hubbard Hamiltonian [see Eq. (D11)] are given by

$$\rho_{\rm Hub}^{S=1,S_z=0}=\frac{1}{2}\begin{array}{c}\begin{array}{cccc}LL & LR & RL & RR\end{array}\\ \begin{pmatrix} 0 & 0 & 0 & 0 \\ & 1 & -1 & 0 \\ & {\rm H.c.} & 1 & 0 \\ & & & 0 \end{pmatrix}\begin{array}{c}LL\\LR\\RL\\RR\end{array}\end{array}, \tag{D36}$$

$$\eta_{\rm Hub}^{S=1,S_z=0}(k_1,k_2)=\frac{4s^2e^{-2s^2(k_1^2+k_2^2)}}{\pi}\begin{array}{c}\begin{array}{cccc}LL & LR & RL & RR\end{array}\\ \begin{pmatrix} 0 & 0 & 0 & 0 \\ & \frac{1}{4} & -\frac{1}{4}e^{-2id(k_1-k_2)} & 0 \\ & {\rm H.c.} & \frac{1}{4} & 0 \\ & & & 0 \end{pmatrix}\begin{array}{c}LL\\LR\\RL\\RR\end{array}\end{array}. \tag{D37}$$

5. Second-excited state

$\rho_{\rm Hub}^{S=0,S_z=0}$ and $\eta_{\rm Hub}^{S=0,S_z=0}(k_1,k_2)$ for the second-excited state of the Hubbard Hamiltonian [see Eq. (D12)] are given by

$$\rho_{\rm Hub}^{S=0,S_z=0}=\frac{1}{2}\begin{array}{c}\begin{array}{cccc}LL & LR & RL & RR\end{array}\\ \begin{pmatrix} 1 & 0 & 0 & -1 \\ & 0 & 0 & 0 \\ & {\rm H.c.} & 0 & 0 \\ & & & 1 \end{pmatrix}\begin{array}{c}LL\\LR\\RL\\RR\end{array}\end{array}, \tag{D38}$$

$$\eta_{\mathrm{Hub}}^{S=0,S_z=0}(k_1,k_2)=\frac{4s^2e^{-2s^2(k_1^2+k_2^2)}}{\pi}\begin{array}{c}\begin{matrix}LL & LR & RL & RR\end{matrix}\\ \begin{pmatrix}\frac{1}{4} & 0 & 0 & -\frac{1}{4}e^{-2id(k_1+k_2)}\\ & 0 & 0 & 0\\ & \mathrm{H.c.} & 0 & 0\\ & & & \frac{1}{4}\end{pmatrix}\end{array}\begin{matrix}LL\\LR\\RL\\RR\end{matrix}. \tag{D39}$$

6. Third-excited state

$\rho_{\mathrm{H}}^{S=0,S_z=0}$ and $\eta_{\mathrm{Hub}}^{S=0,S_z=0}(k_1,k_2)$ for the third-excited state of the Hubbard Hamiltonian [see Eq. (D13)] are given by

$$\rho_{\mathrm{Hub}}^{S=0,S_z=0}=\frac{1}{16-\mathcal{P}(\mathcal{U})\mathcal{U}}\begin{array}{c}\begin{matrix}LL & LR & RL & RR\end{matrix}\\ \begin{pmatrix}4 & -\mathcal{P}(\mathcal{U}) & -\mathcal{P}(\mathcal{U}) & 4\\ & 4-\frac{\mathcal{P}(\mathcal{U})\mathcal{U}}{2} & 4-\frac{\mathcal{P}(\mathcal{U})\mathcal{U}}{2} & -\mathcal{P}(\mathcal{U})\\ & \mathrm{H.c.} & 4-\frac{\mathcal{P}(\mathcal{U})\mathcal{U}}{2} & -\mathcal{P}(\mathcal{U})\\ & & & 4\end{pmatrix}\end{array}\begin{matrix}LL\\LR\\RL\\RR\end{matrix} \tag{D40}$$

$$=\begin{array}{c}\begin{matrix}LL & LR & RL & RR\end{matrix}\\ \begin{pmatrix}C(\mathcal{U})^2 & -C(\mathcal{U})D(\mathcal{U}) & -C(\mathcal{U})D(\mathcal{U}) & C(\mathcal{U})^2\\ & D(\mathcal{U})^2 & D(\mathcal{U})^2 & -C(\mathcal{U})D(\mathcal{U})\\ & \mathrm{H.c.} & D(\mathcal{U})^2 & -C(\mathcal{U})D(\mathcal{U})\\ & & & C(\mathcal{U})^2\end{pmatrix}\end{array}\begin{matrix}LL\\LR\\RL\\RR\end{matrix}, \tag{D41}$$

where $\mathcal{U}=U/t$ and $\mathcal{P}(\mathcal{U})=\sqrt{16+\mathcal{U}^2}-\mathcal{U}$; and

$$\eta_{\mathrm{Hub}}^{S=0,S_z=0}(k_1,k_2)=\frac{2s^2e^{-2s^2(k_1^2+k_2^2)}}{\pi[\mathcal{P}(\mathcal{U})U-16]}\begin{array}{c}\begin{matrix}LL & LR & RL & RR\end{matrix}\\ \begin{pmatrix}4 & -e^{-2idk_2}\mathcal{P}(\mathcal{U}) & -e^{-2idk_1}\mathcal{P}(\mathcal{U}) & 4e^{-2id(k_1+k_2)}\\ & 4-\frac{\mathcal{P}(\mathcal{U})\mathcal{U}}{2} & -\frac{1}{2}e^{-2id(k_1-k_2)}[\mathcal{P}(\mathcal{U})U-8] & -e^{-2idk_1}\mathcal{P}(\mathcal{U})\\ & \mathrm{H.c.} & 4-\frac{\mathcal{P}(\mathcal{U})\mathcal{U}}{2} & -e^{-2idk_2}\mathcal{P}(\mathcal{U})\\ & & & 4\end{pmatrix}\end{array}\begin{matrix}LL\\LR\\RL\\RR\end{matrix}. \tag{D42}$$

[1] S. Fölling, F. Gerbier, A. Widera, O. Mandel, T. Gericke, and I. Bloch, Spatial quantum noise interferometry in expanding ultracold atom clouds, Nature (London) **434**, 481 (2005).

[2] T. Rom, Th. Best, D. van Oosten, U. Schneider, S. Fölling, B. Paredes, and I. Bloch, Free fermion antibunching in a degenerate atomic Fermi gas released from an optical lattice, Nature (London) **444**, 733 (2006).

[3] A. M. Kaufman, B. J. Lester, C. M. Reynolds, M. L. Wall, M. Foss-Feig, K. R. A. Hazzard, A. M. Rey, and C. A. Regal, Two-particle quantum interference in tunnel-coupled optical tweezers, Science **345**, 306 (2014).

[4] B. Fang, A. Johnson, T. Roscilde, and I. Bouchoule, Momentum-Space Correlations of a One-Dimensional Bose Gas, Phys. Rev. Lett. **116**, 050402 (2016).

[5] S. S. Hodgman, R. I. Khakimov, R. J. Lewis-Swan, A. G. Truscott, and K. V. Kheruntsyan, Solving the Quantum Many-Body Problem via Correlations Measured with a Momentum Microscope, Phys. Rev. Lett. **118**, 240402 (2017).

[6] M. Bonneau, W. J. Munro, K. Nemoto, and J. Schmiedmayer, Characterizing two-particle entanglement in a double-well potential, arXiv:1711.08977.

[7] A. Bergschneider, Strong correlations in few-fermion systems, Ph.D. dissertation, Ruperto-Carola University of Heidelberg, 2017, doi:10.11588/heidok.00023328.

[8] P. Treutlein, T. Steinmetz, Y. Colombe, B. Lev, P. Hommelhoff, J. Reichel, M. Greiner, O. Mandel, A. Widera, T. Rom, I. Bloch, and Th.W. Hänsch, Quantum information processing in optical lattices and magnetic microtraps, Fortschr. Phys. **54**, 702 (2006).

[9] R. Islam, R. Ma, Ph.M. Preiss, M. E. Tai, A. Lukin, M. Rispoli, and M. Greiner, Measuring entanglement entropy in a quantum many-body system, Nature (London) **528**, 77 (2015).

[10] B. Paredes, A. Widera, V. Murg, O. Mandel, S. Fölling, I. Cirac, G. V. Shlyapnikov, Th.W. Hänsch, and I. Bloch, Tonks-Girardeau gas of ultracold atoms in an optical lattice, Nature (London) **429**, 277 (2004).

[11] B. B. Brandt, C. Yannouleas, and U. Landman, Two-point momentum correlations of few ultracold quasi-one-dimensional trapped fermions: Diffraction patterns, Phys. Rev. A **96**, 053632 (2017).

[12] G. Zürn, F. Serwane, T. Lompe, A. N. Wenz, M. G. Ries, J. E. Bohn, and S. Jochim, Fermionization of Two Distinguishable Fermions, Phys. Rev. Lett. **108**, 075303 (2012).

[13] S. Murmann, A. Bergschneider, V. M. Klinkhamer, G. Zürn, T. Lompe, and S. Jochim, Two Fermions in a Double Well: Exploring a Fundamental Building Block of the Hubbard Model, Phys. Rev. Lett. **114**, 080402 (2015).

[14] B. B. Brandt, C. Yannouleas, and U. Landman, Double-well ultracold-fermions computational microscopy: Wave-function anatomy of attractive-pairing and Wigner-molecule entanglement and natural orbitals, Nano Lett. **15**, 7105 (2015).

[15] C. K. Hong, Z. Y. Ou, and L. Mandel, Measurement of Subpicosecond Time Intervals Between Two Photons by Interference, Phys. Rev. Lett. **59**, 2044 (1987).

[16] Z. Y. Ou, Multi-photon interference and temporal distinguishability of photons, Int. J. Mod. Phys. **21**, 5033 (2007).

[17] R. C. Liu, B. Odom, Y. Yamamoto, and S. Tarucha, Quantum interference in electron collision, Nature (London) **391**, 263 (1998).

[18] E. Bocquillon, V. Freulon, J.-M. Berroir, P. Degiovanni, B. Plaçais, A. Cavanna, Y. Jin, and G. Fève, Coherence and indistinguishability of single electrons emitted by independent sources, Science **339**, 1054 (2013).

[19] R. Lopes, A. Imanaliev, A. Aspect, M. Cheneau, D. Boiron, and C. I. Westbrook, Atomic Hong-Ou-Mandel experiment, Nature (London) **520**, 66 (2015).

[20] C. Yannouleas, B. B. Brandt, and U. Landman, Ultracold few fermionic atoms in needle-shaped double wells: Spin chains and resonating spin clusters from microscopic Hamiltonians emulated via antiferromagnetic Heisenberg and t-J models, New J. Phys. **18**, 073018 (2016).

[21] P.-O. Löwdin and H. Shull, Natural orbitals in the quantum theory of two-electron systems, Phys. Rev. **101**, 1730 (1956).

[22] J. Li, M.-T. Zhou, B. Jing, X.-J. Wang, S.-J. Yang, X. Jiang, K. Mølmer, X.-H. Bao, and J.-W. Pan, Hong-Ou-Mandel Interference Between Two Deterministic Collective Excitations in an Atomic Ensemble, Phys. Rev. Lett. **117**, 180501 (2016).

[23] M. D. Girardeau, Two super-Tonks-Girardeau states of a trapped one-dimensional spinor Fermi gas, Phys. Rev. A **82**, 011607(R) (2010).

[24] T. Jeltes, J. M. McNamara, W. Hogervorst, W. Vassen, V. Krachmalnicoff, M. Schellekens, A. Perrin, H. Chang, D. Boiron, A. Aspect, and C. I. Westbrook, Comparison of the Hanbury Brown-Twiss effect for bosons and fermions, Nature (London) **445**, 402 (2007).

[25] Z. Y. Ou and L. Mandel, Observation of Spatial Quantum Beating with Separated Photodetectors, Phys. Rev. Lett. **61**, 54 (1988).

[26] E. Altman, E. Demler, and M. D. Lukin, Probing many-body states of ultracold atoms via noise correlations, Phys. Rev. A **70**, 013603 (2004).

[27] Y. M. Blanter and M. Büttiker, Shot noise in mesoscopic conductors, Phys. Rep. **336**, 1 (2000).

[28] The preparatory measurements were performed for three different interaction strengths, $U = 0$ (noninteracting), $U/t = 2.1$ (weak strength), and $U/t = 7.7$ (intermediate strength); see Fig. 7. 8(a)–(c) in Ref. [7]. In the absence of the present CI results and the Hubbard-type formula in Eq. (5), no analysis of the full correlation maps and their interference patterns was carried out in Ref. [7].

[29] R. Žitko, SNEG–Mathematica package for symbolic calculations with second-quantization-operator expressions, Comput. Phys. Commun. **182**, 2259 (2011).

[30] Computer code MATHEMATICA (Wolfram Research, Version 11.2, Champaign, IL, 2017).

[31] C. Yannouleas and U. Landman, Symmetry breaking and quantum correlations in finite systems: Studies of quantum dots and ultracold Bose gases and related nuclear and chemical methods, Rep. Prog. Phys. **70**, 2067 (2007).

[32] Y. Li, C. Yannouleas, and U. Landman, Artificial quantum-dot helium molecules: Electronic spectra, spin structures, and Heisenberg clusters, Phys. Rev. B **80**, 045326 (2009).

[33] J. Schliemann, D. Loss, and A. H. MacDonald, Double-occupancy errors, adiabaticity, and entanglement of spin qubits in quantum dots, Phys. Rev. B **63**, 085311 (2001).

[34] K. Eckert, J. Schliemann, D. Bruß, and M. Lewenstein, Quantum correlations in systems of indistinguishable particles, Ann. Phys. (NY) **299**, 88 (2002).